International Journal of Heat and Fluid Flow 103 (2023) 109187

Contents lists available at ScienceDirect

International Journal of Heat and Fluid Flow

journal homepage: www.elsevier.com/locate/ijhff

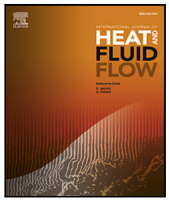

Large-eddy simulation of free-surface turbulent channel flow over square bars

Razieh Jalalabadi *, Thorsten Stoesser

Civil, Environmental and Geomatic Engineering, University College London, London, WC1E 6BT, UK

ARTICLE INFO

Keywords:
Free-surface turbulent channel flow
Large-eddy simulation
Rough-bed
Shear stress budget
Kinetic energy budget

ABSTRACT

The results of large-eddy simulations of free-surface turbulent channel flow over spanwise-aligned square bars are used to investigate the effects of bed roughness and water surface deformations on the root-mean-squared velocity fluctuations, dispersive shear stress, double-averaged Reynolds shear stress, wake kinetic energy and double-averaged turbulent kinetic energy. Two bar spacings, corresponding to transitional and k-type roughness, at similar Reynolds and Froude numbers are considered. The main peak of all statistical quantities occurs at the bar crest height. The effects of a standing wave at the water surface in flow over k-type roughness is marked by a local peak under the water surface for all statistical quantities considered here except wall-normal and spanwise velocity fluctuations. Quadrant analysis shows that sweeps and ejections are the strongest events contributing to both dispersive and double-averaged Reynolds shear stress but their contributions are different for the two bar spacings. Examining the budgets of dispersive and double-averaged Reynolds shear stress reveals that the dominant terms of these stresses are pressure–strain correlation and pressure transport and the contribution of wake production is similar for both of these stresses but with opposite sign. In addition to the main role of the bars in consuming or producing wake kinetic energy through production and transport and convection, the standing wave at the water surface in flow over k-type roughness induces large convection in the bulk flow too. The dominant terms in the double-averaged turbulent kinetic energy budget are similarly production, transport and convection. Large shear production renders large temporal fluctuations than spatial fluctuations of flow variables. The interaction of bars, bed and water surface is seen in the convection term in flow over k-type roughness.

1. Introduction

Turbulent open channel flow over rough surfaces is ubiquitous in nature and man-made geometries such as rivers, sewerage systems and canals. The interaction of water surface and bed roughness with bulk flow enhances the complexity of flow dynamics and energy and momentum exchange. Scrutinizing flow statistics in this type of flow and their contribution to flow characteristics and quantities, such as friction coefficient and momentum and energy transport, reveals the effects of water surface and bed roughness on flow hydrodynamics and provides deep insights for engineering and research applications.

Surface roughness in wall-bounded flows leads to modulation of flow quantities and their distributions from the viscous to the overlap layer depending on the height of the roughness (Jiménez, 2004). Roughness topography is one of the deterministic factors governing the changes in the flow. In shallow open channel flows the alterations made by bed roughness in the flow are extended to the water surface. To account for the effects of bed roughness on the averaged parameters the double averaging method was introduced (Wilson and Shaw, 1977; Raupach and Shaw, 1982). In this approach the governing fluid flow equations are averaged first temporally and then spatially. The resulting double-averaged Navier–Stokes (DANS) equations include temporal variations of flow variables and spatial variations of time-averaged flow variables (Nikora et al., 2007). These spatial variations are induced by near-bed flow heterogeneity and secondary currents. In analogy to time-averaged quantities, second order statistics such as wake kinetic energy (WKE) and dispersive shear stress (DSS) are interoduced due to the spatial variations of flow variables. The total kinetic energy is the sum of wake, turbulent and mean kinetic energy (Raupach and Shaw, 1982; Papadopoulos et al., 2019; Zampiron et al., 2021), and the dispersive shear stress contributes to the flow dynamics through turbulent inertia term in DANS (Manes et al., 2008; Jelly and Busse, 2019; Jalalabadi and Stoesser, 2022). The spatial variations of mean flow variables are generally small compared to time-averaged variations; however, for some rough surfaces they can contribute substantially to

* Corresponding author.
E-mail addresses: r.jalalabadi@ucl.ac.uk (R. Jalalabadi), t.stoesser@ucl.ac.uk (T. Stoesser).

https://doi.org/10.1016/j.ijheatfluidflow.2023.109187
Received 30 January 2023; Received in revised form 7 June 2023; Accepted 16 June 2023
Available online 18 July 2023

momentum transfer or losses (Forooghi et al., 2018; Jelly and Busse, 2019; Toussaint et al., 2020). While the magnitude of Reynolds normal and shear stresses are non-negligible at all wall-normal distances in the flow, the magnitude of dispersive stresses is negligible far above the roughness crest and their peak occur under or around the roughness crest. In free surface flows, the variations of free surface elevation induce spatial variations in flow variables as well (Jalalabadi and Stoesser, 2022).

The roughness geometry is an important factor affecting various flow features close to the wall while the bulk flow far from the roughness crest experiences similar alteration for various roughness shapes especially when the maximum roughness height is negligible compared to the integral length scale of the flow. Among different roughness geometries, square bars orientated perpendicular to the main flow direction have been applied in numerous researches with the aim to study principle effects of surface roughness on flow characteristics (Djenidi et al., 1999; Cui et al., 2003; Krogstad et al., 2005; Ikeda and Durbin, 2007). Different types of this roughness geometry are defined based on the bar spacing which dictates the drag increment due to the roughness (Jiménez, 2004). The main two types of this roughness are d-type and k-type where in the d-type roughness a stable vortex is formed between the bars but in the k-type roughness the flow reattaches to bed after a recirculation zone at downstream of bars. The transition from d-type to k-type roughness occurs at $\lambda/k = 4-5$ where λ is the bar spacing and k is the bar height (Jiménez, 2004).

Investigating the budgets of kinetic energy and shear stress reveals the process of generation, cascade and dissipation of energy and exchange of momentum and scalars in turbulent flows. The results have been applicable in formulating Reynolds-averaged turbulent models to predict turbulent flows as well (Mansour et al., 1988). In wall-bounded turbulent flows the inhomogeneity near the wall makes the theoretical understanding of the physics of turbulent flow challenging (Hoyas and Jiménez, 2008) especially when roughness is attached to the wall to generate the real physical condition. Although being helpful in elucidating major flow phenomena occurring in turbulent flows, experimental studies have restraints in determining the exact contribution of all terms in the budget equations especially dissipation and pressure transport. In the first numerical work revealing the contribution of involved terms in budgets of Reynolds shear stress (RSS) and turbulent kinetic energy (TKE) in smooth channel, all terms were shown to be important near the wall (Mansour et al., 1988). Further studies at larger Reynolds numbers of turbulent flow in smooth channel presented similar results (Antonia and Kim, 1994; Abe et al., 2001; Coleman et al., 2003). Spalart (1988) and Hoyas and Jiménez (2008) reported the budgets of Reynolds normal and shear stress and TKE for turbulent smooth boundary layer and channel flow respectively and discussed the effects of different normalizations. Komminaho and Skote (2002) provided the results comparing the budgets of Reynolds normal and shear stress for rotating and non-rotating couette flow and boundary layer with zero and adverse pressure gradient all over smooth wall. Several studies that have analysed TKE budget experimentally (Nezu and Nakagawa, 1993; Castro et al., 2006; Blackman et al., 2017) and numerically (Ashrafian and Andersson, 2006; Tian et al., 2020; Orlandi and Pirozzoli, 2021) in flow over rough surfaces, including plant canopy and urban canopy flows, have summarized the effects of roughness on TKE budget terms. In these studies the components of TKE budget were first calculated for the TKE transport equation and then each component was averaged spatially in homogeneous directions. However, double-averaged turbulent kinetic energy (DATKE) transport equation is derived using DANS hence the equation contains spatial variations of time-averaged flow variables and some new terms that represent the near-bed flow heterogeneity. DATKE budget contributions have been presented in few works including Dwyer et al. (1997), Finnigan (2000), Yuan and Piomelli (2014), Giometto et al. (2016), Papadopoulos et al. (2019) and Zampiron et al. (2021) and in the last two works the interaction of WKE and DATKE have been studied. The dispersive normal stresses budgets have been examined in Yuan and Piomelli (2014) while, to the authors' knowledge, the dispersive shear stress (DSS) budget and its interaction with double-averaged Reynolds shear stress (DARSS) have not yet been demonstrated.

The present work investigates free-surface turbulent flow over transitional and k-type square-bar roughness at moderate Reynolds and Froude numbers. Considering the significant effects of bed roughness on the distribution of first and second order statistics as well as turbulent flow structures, the root-mean-squared velocity fluctuations, shear stresses and kinetics energies are presented based on the results of large-eddy simulation. Quadrant analysis is applied to reveal the contribution of different turbulent events on dispersive and double-averaged Reynolds shear stresses. The transport equations of shear stresses and kinetic energies are presented and their contributions are scrutinized to explore their dependency on bed roughness and water surface deformations. In Section 2 the details of numerical simulations and double-averaging methodology are described. Section 3 presents and discusses the results and the conclusion is presented in Section 4.

2. Numerical setup and double-averaging methodology

The in-house LES code Hydro3D is employed which has been validated for a large number of flows with similar complexity (Kara et al., 2015; McSherry et al., 2018). The code solves the spatially filtered Navier–Stokes equations

$$\nabla \cdot \mathbf{u} = 0 \tag{1}$$

$$\frac{\partial \mathbf{u}}{\partial t} + \mathbf{u} \cdot \nabla \mathbf{u} = -\nabla p + \frac{1}{Re}\nabla^2 \mathbf{u} - \nabla \cdot \tau \tag{2}$$

where $\mathbf{u} = (u, v, w)$ is the velocity vector with the components in the streamwise (x), spanwise (y) and wall-normal (z) directions, p is the pressure and τ is the subgrid scale stress tensor. A fractional-step method is applied on a staggered Cartesian grid where in the predictor step a second order Runge–Kutta scheme is applied to predict the velocities. In the corrector step the pressure Poisson equation is solved using a multi-grid method to achieve a divergence-free flow field. The diffusive terms are computed using second order finite difference scheme and the convective terms are computed using a fifth-order weighted, essentially non-oscillatory (WENO) scheme to improve algorithm stability (Kara et al., 2015). The Wall-Adapting Local Eddy-viscosity (WALE) model is used to calculate eddy viscosity (Nicoud and Ducros, 1999). The free surface is captured using the Level Set Method (Sethian and Smereka, 2003). In this method the interface is tracked by solving a pure advection equation for a level set signed distance function. This function is zero at the phase interface, negative in air and positive in water. As there is a numerical instability due to sudden change and discontinuity of density and viscosity of the two immiscible fluids at the interface, a transition zone is introduced at its either side. In the transition zone, with the thickness of two grid spacing, density and viscosity are calculated using a Heaviside function. The governing equations are solved via parallel computing using Message Passing Interface (MPI). Table 1 provides hydraulic parameters of the simulations. The λ/k = 5.2 case is transitional (wake interference flow) roughness, while the λ/k = 10.4 case is classified as k-type roughness. The global Froude number, $Fr = U_b/\sqrt{gH}$, and Reynolds number, $Re = U_b H/\nu$, are kept constant for all cases where U_b is the bulk velocity calculated as the average velocity in the channel which gives the mass flow rate similar to experiments in McSherry et al. (2018), H is the depth defined as the distance between the mean water surface position before starting the simulation and the mean bed elevation (see Fig. 1), ν is the fluid kinematic viscosity and g is the gravity acceleration. Small differences in Re and Fr are due to carrying out the simulations using constant pressure gradient. The superscript + represents the inner-scaled quantities calculated using the friction velocity $u_\tau = \sqrt{\tau_{\text{wall}}/\rho}$ where τ_{wall} is the wall shear stress calculated using the velocity gradient adjacent to the wall above and between the bars and averaged in the streamwise

Table 1
Hydraulic conditions and grid resolution.

λ/k	H/k	U_b	Re	Fr	Δx^+, Δy^+, Δz^+
5.2	2.5	0.24	7.2×10^3	0.44	5.6,6.6,3.5
10.4	2.9	0.23	8.0×10^3	0.39	5.5,6.5,3.5

direction and ρ is the water density. Fig. 1 presents the schematic of the computational domain. The domain size is similar for both bar spacing and equal to $10.4k \times 5k \times 5k$ in the x, y and z directions respectively. Hence, for the $\lambda/k = 5.2$ case the domain includes two troughs while for $\lambda/k = 10.4$ it only contains one trough. The boundary conditions include periodic condition in the streamwise and spanwise directions and a no-slip boundary condition at the bed and at the surface of the bars where the latter is met by setting the velocity at the first grid point inside the bar equal to the negative value of that at the first grid point outside the bar in every time step thus the velocity is exactly zero at the boundary. The simulations in this work are initiated with a free-slip boundary condition at the water level and after attaining a fully developed flow this boundary condition is removed so the water surface is tracked by the level set algorithm. After achieving fully developed flow, averaging of the flow quantities is begun. The present simulations were validated rigorously in Jalalabadi et al. (2021) using the numerical and experimental results reported in McSherry et al. (2018). Both flows presented were simulated using two grid resolutions (current grid and a finer grid). The simulations on the finer grid, which consisted of twice the number of grid points in all spatial directions than the grids used here, only provided very minor differences in terms of turbulence statistics, and simulations on both grids showed very convincing agreement with experimental data. A regular and a large domain with twice the size in both streamwise and spanwise directions were tested too. Flow statistics and water surface elevations of the domain used here were in very good agreement with both the experimental data and the results of the large domain. In addition, two-point correlation of the streamwise velocity fluctuations in both streamwise and spanwise directions were carried out demonstrating adequacy of the domain size as well.

In this work, small symbols are instantaneous quantities, small symbols with prime are temporal fluctuations, time-averaged quantities are denoted with an overbar and spatially averaged quantities are denoted with brackets $\langle\rangle$ thus the double-averaged quantities are denoted by both the overbar and brackets and the spatial fluctuations of the time-averaged quantities are denoted by a tilde. An instantaneous flow variable is written as the sum of double-averaged, temporal and spatial fluctuations of that variable as

$$\theta(x,y,z,t) = \left\langle \overline{\theta} \right\rangle (z) + \widetilde{\theta}(x,y,z) + \theta'(x,y,z,t) \tag{3}$$

while a double-averaged variable is calculated using the volume-averaging operator applied to the temporally-averaged variable. The averaging volume should be larger than the dominant roughness scale (Nikora et al., 2007; Pokrajac et al., 2007) hence here it is considered as a thin slab parallel to the bed with the size $L_x \times L_y \times \Delta z$. In this slab, V_o is the total volume and V_f is the volume occupied by the fluid. Geometry function, a parameter used to account for the dependence of double-averaged equations on the roughness geometry, is defined as $\phi = V_f / V_o$. Volume averaging is defined as

$$\langle\theta\rangle(z) = \frac{1}{\phi(z)} \frac{1}{V_o} \int\int\int_{V_f} \theta(x,y,z)\, dx\, dy\, dz \tag{4}$$

To Derive the DANS equations proposed in this work one should replace instantaneous flow variables in Eqs. (1) and (2) by $\theta = \overline{\theta} + \theta'$ and apply temporal averaging. In the resulting equations the temporally averaged variables should be replaced by $\overline{\theta} = \langle\overline{\theta}\rangle + \widetilde{\theta}$ and spatial averaging should be applied to the result. The resulting DANS equations

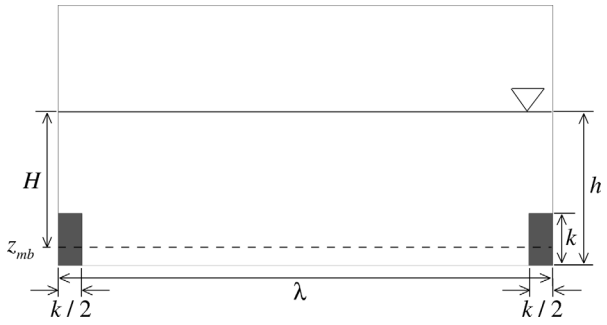

Fig. 1. Schematic of the computational domain.

after simplifications and considering constant ϕ for the roughness shape in the present work is

$$\frac{\partial\langle\overline{u_i}\rangle}{\partial t} + \langle\overline{u_j}\rangle \frac{\partial\langle\overline{u_i}\rangle}{\partial x_j} = -\frac{1}{\rho}\frac{\partial\langle\overline{p}\rangle}{\partial x_i} - \frac{1}{\rho}\langle\frac{\partial\widetilde{p}}{\partial x_i}\rangle - \frac{\partial\left\langle\overline{u_i'u_j'}\right\rangle}{\partial x_j} - \frac{\partial\left\langle\widetilde{u}_i\widetilde{u}_j\right\rangle}{\partial x_j} + \nu\left[\nabla^2\langle\overline{u_i}\rangle + \langle\nabla^2\widetilde{u}_i\rangle\right] \tag{5}$$

This is similar to equation 7 in Raupach and Shaw (1982) but different from the DANS equations derived in Nikora et al. (2007). The reason is that in the latter work DANS equations are derived by averaging individual terms spatially in NS equations using theorems mentioned in that work to perform spatial-averaging of instantaneous variables which is a different approach than the one applied here. The budget equations of shear stresses and kinetic energies in the rest of this work are derived using Eq. (5) thus the definition of terms in them are different from those mentioned in Papadopoulos et al. (2019) and Zampiron et al. (2021) which used DANS calculated in Nikora et al. (2007) to derive similar budgets equations. The dispersive stress is calculated as (Jelly and Busse, 2018)

$$\tilde{u}\tilde{w} = (\overline{u} - \langle\overline{u}\rangle)(\overline{w} - \langle\overline{w}\rangle) \tag{6}$$

where each parentheses on the right hand side represents the spatial fluctuation of a velocity component. The double-averaged total kinetic energy is written as

$$\frac{1}{2}\langle\overline{u_i u_i}\rangle = \left[\frac{1}{2}\langle\overline{u_i}\rangle\langle\overline{u_i}\rangle\right]_{\mathrm{MKE}} + \left[\frac{1}{2}\left\langle\overline{u_i'u_i'}\right\rangle\right]_{\mathrm{DATKE}} + \left[\frac{1}{2}\langle\widetilde{u_i}\widetilde{u_i}\rangle\right]_{\mathrm{WKE}} \tag{7}$$

The distribution of dispersive and Reynolds shear stress in streamwise-wall-normal plane and the contributions of doubled-averaged total kinetic energy have been presented and discussed in Jalalabadi and Stoesser (2022).

3. Results and discussion

Fig. 2 shows vertical profiles of spatially-averaged root-mean-square (rms) velocity fluctuations. The main peak values for these velocities occur at around the bar crest height. There is, as well, a second peak for these velocities under the water surface. One main feature of the water surface in flow over $\lambda/k = 10.4$ is the presence of a standing wave that is generated due to the interaction of bed and water surface and the effects of recirculation zone which is only present in flow over larger bar spacing (Jalalabadi et al., 2021). This standing wave is not developed in flow over $\lambda/k = 5.2$. The second peak of the streamwise component of rms velocities is more noticeable in flow over $\lambda/k = 10.4$ highlighting the effects of this standing wave. These second peaks have similar values and occur at similar z/k for $\langle v_{rms}\rangle^+$ implying that only the water surface presence contributes to the generation of this peak regardless of its specific deformations. The second peaks under the

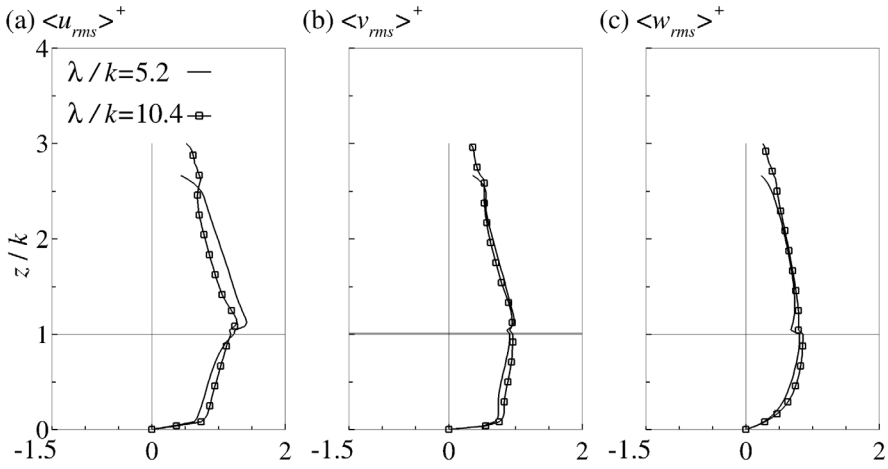

Fig. 2. Spatially-averaged (a) streamwise (b) spanwise (c) wall-normal rms velocity fluctuations for λ/k = 5.2 and λ/k = 10.4.

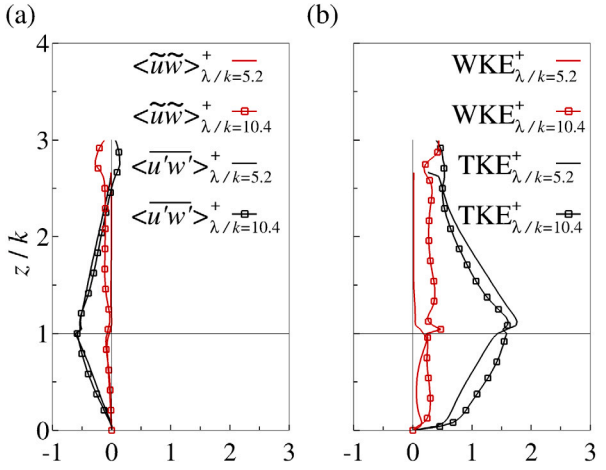

Fig. 3. (a) Double-averaged Reynolds and dispersive shear stress and (b) Double-averaged turbulent and wake kinetic energy for λ/k = 5.2 and λ/k = 10.4.

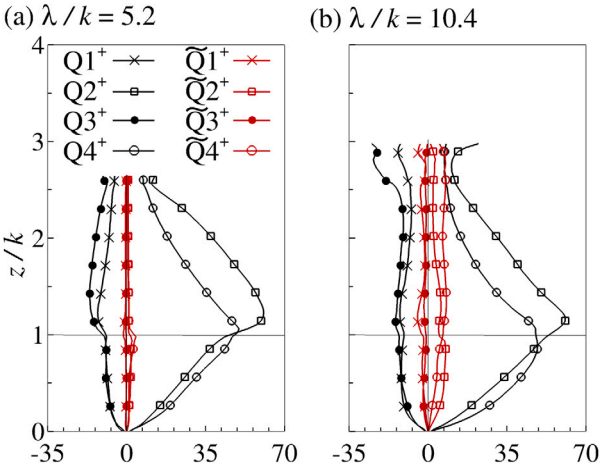

Fig. 4. Quadrant components of Double-averaged Reynolds (black) and dispersive (red) shear stress for (a) λ/k = 5.2 and (b) λ/k = 10.4. (For interpretation of the references to colour in this figure legend, the reader is referred to the web version of this article.)

water surface are weak for $\langle w_{rms}\rangle^+$ rendering the small effects of water surface and its deformations on this component of velocity fluctuations. Under the bar crest all rms velocity fluctuations are larger in flow over λ/k = 10.4 than those in λ/k = 5.2. This is attributed to the presence of a recirculation point after which the flow reattaches to the bed and rms velocity fluctuations experience an increase at smaller z/k. Above the bar crest, on the other hand, the streamwise rms velocity is larger for λ/k = 5.2. This is due to the difference in bar spacing in the two cases considered here. The larger bar spacing for λ/k = 10.4 leads to the generation of a recirculation zone and standing wave at the water surface. At the downstream of the surface standing wave and after the recirculation zone, that occurs at roughly similar x/k, the flow reattaches to the bed and the effects of bars on the bulk flow are diminished (Jalalabadi et al., 2021) thus the streamwise velocity experiences smaller fluctuations above the bar crest. In λ/k = 5.2 the flow is skimmed due to the smaller bar spacing hence the streamwise velocity and its fluctuations dose not experience notable streamwise variations above the bar crest (Jalalabadi et al., 2021) and are large at all x/k making $\langle u_{rms}\rangle^+$ larger in flow over λ/k = 5.2. Similar values of $\langle v_{rms}\rangle^+$ and $\langle w_{rms}\rangle^+$ above the bar crest in both geometries reveal the negligible effects of bar spacing and water surface deformations on the temporal fluctuations of velocity in the spanwise and wall-normal directions.

The normalized double-averaged Reynolds shear stress and turbulent kinetic energy are shown in Fig. 3 along with the dispersive shear stress and wake kinetic energy. DARSS is similar in both geometries with a main peak at around bar crest height except close to the water surface where $\left\langle\overline{u'w'}\right\rangle^+$ experiences a strong positive peak only in flow over λ/k = 10.4. This is due to a local increase in the value of this stress at the downstream of the standing wave (Jalalabadi and Stoesser, 2022). It was shown in Jalalabadi and Stoesser (2022) that the maximum of $\left\langle\overline{u'w'}\right\rangle^+$ occurs at smaller z/k under the bar crest in flow over λ/k = 10.4 than that in λ/k = 5.2 thus DARSS is slightly larger under the bar crest in flow over larger bar spacing and smaller above that. Dispersive shear stress is similar for both roughness spacing under the bar crest and it has a local maxima at the bar crest height. However, above the bar crest $\left\langle\widetilde{u}\widetilde{w}\right\rangle^+$ increases with distance from the bar and exhibits a second peak close to the water surface in flow over λ/k = 10.4 while in flow over λ/k = 5.2 DSS is negligible above the bar crest. In flow over larger bar spacing the surface standing wave contributes to large spatial variations of mean flow quantities while these fluctuations are negligible in flow over smaller bar spacing. Accordingly, DSS has larger contribution to the friction coefficient in flow over λ/k = 10.4 than that in flow over λ/k = 5.2 (Jalalabadi and Stoesser, 2022). The distribution of DATKE is similar to the distribution of velocity rms fluctuations and shear stresses with a main peak at the bar crest height and a second peak close to the water surface only in flow over larger bar spacing. The smaller DATKE above the bar crest and stronger second peak under the water surface in flow over λ/k = 10.4 than those in flow over λ/k = 5.2 are similar to the variations of the streamwsie

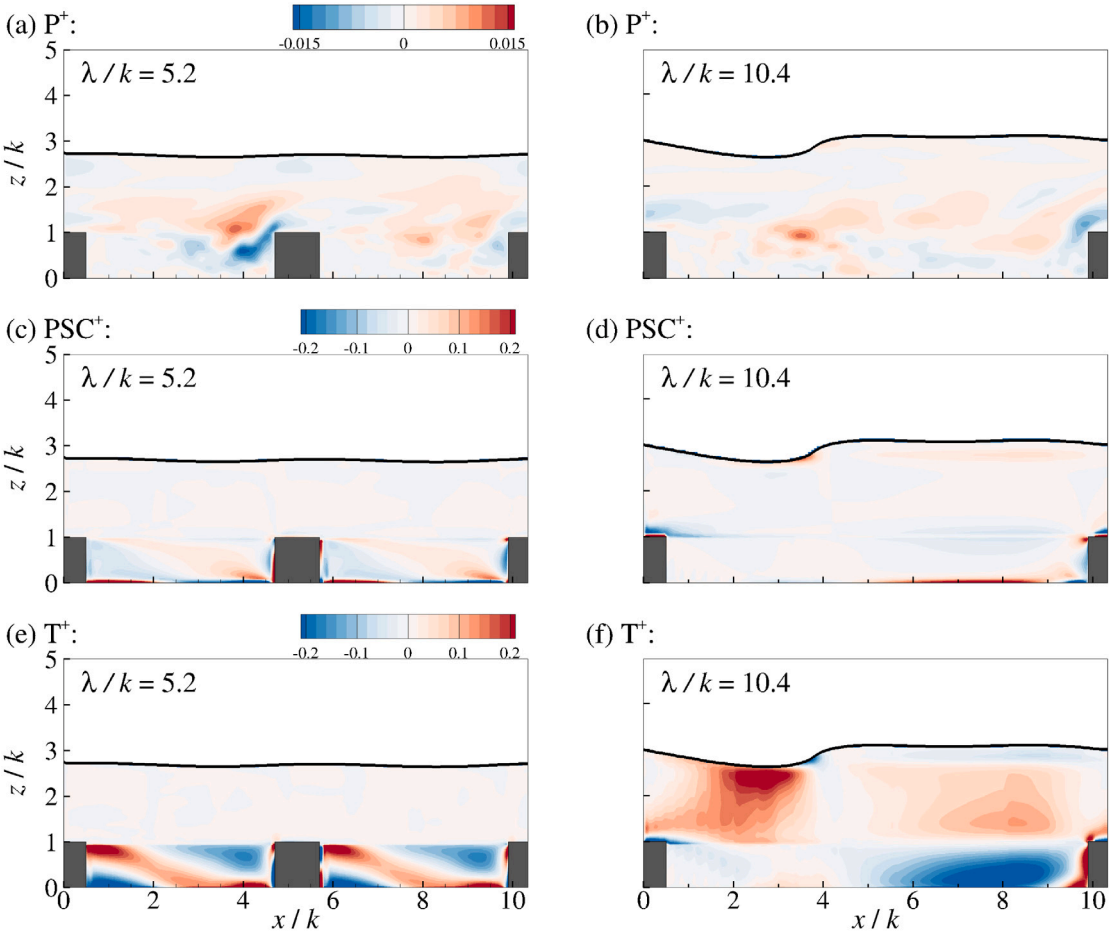

Fig. 5. Dominant terms of dispersive shear stress budget for (a,c,e) $\lambda/k = 5.2$ and (b,d,f) $\lambda/k = 10.4$.

contributor of DATKE as shown in Fig. 2(a). Unlike other variables in Fig. 3, WKE is larger at all wall-normal locations in flow over $\lambda/k = 10.4$ than that in flow over $\lambda/k = 5.2$. The larger WKE and its second peak in flow over larger bar spacing renders the effects of the surface standing wave and roughness spacing in increasing spatial fluctuations of the mean flow quantities.

The contribution of velocity fluctuations to the generation of Reynolds and dispersive shear stresses are shown in Fig. 4. These stresses are divided into four events, Q1 to Q4, based on the sign of their fluctuating components (Wallace, 2016). The second and fourth quadrants, $Q2^+$ and $Q4^+$, correspond to vertical flow away from the wall ($w' > 0$) in the reverse direction of the mean streamwise velocity ($u' < 0$) and towards the wall ($w' < 0$) in the same direction of the mean stremwise velocity ($u' > 0$) and known as ejection and sweep events respectively. As shown in Fig. 4, $Q2^+$ and $Q4^+$ are the dominant events for DARSS in both geometries which is consistent with the previous works for flow above different roughness types (Stoesser and Rodi, 2007) . $Q4^+$ is the strongest under the bar crest height and $Q2^+$ is the strongest above that. This is reversed for DSS in flow over $\lambda/k = 10.4$. This reveals that the sign of spatial fluctuations of streamwise and wall-normal velocities are opposite of the sign of temporal fluctuations of these components. The negligible value of all quadrants of DSS in the flow over $\lambda/k = 5.2$ is similar to the negligible value of this stress in this case (Fig. 3(a)) and due to small spatial fluctuations of velocities in this case. The standing wave at the water surface contributes to the increase in $Q1^+$ to $Q4^+$ under the water surface for $\lambda/k = 10.4$ while in flow over $\lambda/k = 5.2$ this increase is mild.

To sum, the fluctuations of velocities, shear stresses and kinetic energies were shown to examine the effects of bars and water surface deformations on these flow variables. The effects of water surface standing wave in flow over large bar spacing was local in DARSS and DATKE under the water surface while its effects on the DSS and WKE was extended down towards the bed. The budgets of DARSS, DSS, DATKE and WKE will be shown in next sections to discuss the dominant terms contributing to these second order statistics and explore how they depend on roughness spacing and water surface deformations.

3.1. Dispersive shear stress and double-averaged Reynolds shear stress budget

The budgets of dispersive shear stress and double-averaged Reynolds shear stress are as follows

$$\begin{aligned}\frac{\partial\langle\widetilde{u}_i\widetilde{u}_k\rangle}{\partial t} &= \left[-\langle\overline{u}_j\rangle\frac{\partial\langle\widetilde{u}_i\widetilde{u}_k\rangle}{\partial x_j}\right]_{\mathrm{C}} \\ &+\left[\left(-\langle\widetilde{u}_k\widetilde{u}_j\rangle\frac{\partial\langle\overline{u}_i\rangle}{\partial x_j}-\langle\widetilde{u}_i\widetilde{u}_j\rangle\frac{\partial\langle\overline{u}_k\rangle}{\partial x_j}\right)_{\mathrm{P_s}}\right. \\ &\left.+\left(\langle\widetilde{u_i'u_j'}\frac{\partial\widetilde{u}_k}{\partial x_j}\rangle+\langle\widetilde{u_k'u_j'}\frac{\partial\widetilde{u}_i}{\partial x_j}\rangle\right)_{\mathrm{P_w}}\right]_{\mathrm{P}} \\ &+\left[-2\nu\langle\frac{\partial\widetilde{u}_i}{\partial x_j}\frac{\partial\widetilde{u}_k}{\partial x_j}\rangle\right]_{\varepsilon} \\ &+\left[\frac{1}{\rho}(\langle\widetilde{p}\frac{\partial\widetilde{u}_k}{\partial x_i}\rangle+\langle\widetilde{p}\frac{\partial\widetilde{u}_i}{\partial x_k}\rangle)\right]_{\mathrm{PSC}} \\ &+\left[\left(-\frac{\partial\langle\widetilde{u}_i\widetilde{u}_j\widetilde{u}_k\rangle}{\partial x_j}\right)_{\mathrm{T_d}}\right. \\ &\left.+\left(-\langle\frac{\partial\widetilde{u_i'u_j'}\widetilde{u}_k}{\partial x_j}\rangle-\langle\frac{\partial\widetilde{u_k'u_j'}\widetilde{u}_i}{\partial x_j}\rangle\right)_{\mathrm{T_w}}\right.\end{aligned}$$

$$\left(-\frac{1}{\rho}(\langle\frac{\partial\widetilde{p}\widetilde{u_k}}{\partial x_i}\rangle+\langle\frac{\partial\widetilde{p}\widetilde{u_i}}{\partial x_k}\rangle)\right)_{T_p}+\left(\nu\left\langle\nabla^2\widetilde{u_i}\widetilde{u_k}\right\rangle\right)_{T_v}\Bigg]_T \tag{8}$$

$$\begin{aligned}\frac{\partial\langle\overline{u_i'u_k'}\rangle}{\partial t}=&\left[-\langle\overline{u_j}\rangle\frac{\partial\langle\overline{u_i'u_k'}\rangle}{\partial x_j}\right]_C\\&+\left[\left(-\langle\overline{u_k'u_j'}\rangle\frac{\partial\langle\overline{u_i}\rangle}{\partial x_j}-\langle\overline{u_i'u_j'}\rangle\frac{\partial\langle\overline{u_k}\rangle}{\partial x_j}\right)_{P_s}\right.\\&\left.\left(-\langle\widetilde{u_i'u_j'}\frac{\partial\widetilde{u_k}}{\partial x_j}\rangle-\langle\widetilde{u_k'u_j'}\frac{\partial\widetilde{u_i}}{\partial x_j}\rangle\right)_{P_w}\right]_P\\&+\left[-2\nu\langle\overline{\frac{\partial u_i'}{\partial x_j}\frac{\partial u_k'}{\partial x_j}}\rangle\right]_\varepsilon\\&+\left[\frac{1}{\rho}(\langle p'\overline{\frac{\partial u_k'}{\partial x_i}}+p'\overline{\frac{\partial u_i'}{\partial x_k}}\rangle)\right]_{PSC}\\&+\left[\left(-\frac{\partial\langle\overline{u_j'u_j'u_k'}\rangle}{\partial x_j}\right)_{T_t}\right.\\&+\left(-\langle\frac{\partial\widetilde{u_j}\widetilde{u_i'u_k'}}{\partial x_j}\rangle\right)_{T_w}\\&\left(-\frac{1}{\rho}(\frac{\partial\langle p'u_k'\rangle}{\partial x_i}+\frac{\partial\langle p'u_i'\rangle}{\partial x_k})\right)_{T_p}\\&\left.+\left(\nu\langle\nabla^2\overline{u_i'u_k'}\rangle\right)_{T_v}\right]_T\end{aligned} \tag{9}$$

Eqs. (8) and (9) are derived by the present authors using mathematical operations on Reynolds- and double-averaged Navier–Stokes equations and simplifications of the resulting equations using Eq. (3) and considering constant ϕ for the roughness shape here. The definition of the budget terms in these equations are similar to the classical definition of Reynolds shear stress budgets with the four terms of production, dissipation, transport and convection. However, these equations are different from the corresponding ones mentioned in Papadopoulos et al. (2019) and Zampiron et al. (2021) as they used different form of DANS and a different approach for derivation of these budgets and definition of budget terms. Fig. 5 presents the budgets of DSS, $\langle\widetilde{u}\widetilde{w}\rangle^+$, calculated using Eq. (8) for $i=1$ and $k=3$ (streamwise and wall-normal directions respectively) for both bar spacings. All terms in this section are normalized by ${u_\tau}^3/H$ to account for the effects of flow submergence on the contributions to DSS and DARSS near and far from the bed. In both geometries the dissipation (ε^+) and convection (C^+) terms are negligible and not shown. Production (P^+) is shown, although being considerably smaller than the dominant terms, to evaluate the effects of bars on this term which is a major source for the Reynolds shear stress (Mansour et al., 1988; Spalart, 1988; Hoyas and Jiménez, 2008). Pressure–strain correlation (PSC^+) and transport (T^+) terms are the two dominant ones. The dominant production term for DSS in the present work is wake production (P_w in Eq. (8)) which is generated due to the drag imposed by the bars and turbulent motion in the wake of them. Due to homogeneity of roughness geometry in the spanwise direction mean velocity gradients in this direction are negligible making ${P_s}^+$ a minor contribution to P^+. Thus the total production terms shown in Fig. 5(a,b) are roughly equal to ${P_w}^+$. In flow over $\lambda/k=5.2$ there are only two regions of notable ${P_w}^+$ generated side by side close to the leading edge of the bars. These regions have opposite signs, positive and negative which are source and loss of DSS respectively, making the streamwise-averaged ${P_w}^+$ negligible. In flow over $\lambda/k=10.4$ there are similar regions but the source of ${P_w}^+$ is generated roughly above the reattachement point (Jalalabadi et al., 2021) while the loss occurs at the leading edge of the bars and similar to smaller bar spacing the streamwise-averaged ${P_w}^+$ is negligible. In both geometries, Pressure–strain correlation is significant close to the bed and edges of the bars due to the large pressure variations in these areas. In flow over $\lambda/k=5.2$, the regions of strong PSC^+ close to the bed and the two regions of relatively large PSC^+ between the bars and under their crest counterbalance each other in the streamwise direction. The effects of larger bar spacing is clear in Fig. 5(d) where PSC^+ is negligible close to the bed under the recirculation zone ($x/k<5$) but it is significant at the downstream of this zone making the streamwise-averaged PSC^+ relatively large close to the bed. In this geometry pressure–strain correlation is large, as well, just above the bar since unlike Fig. 5(c) the flow is not skimmed here and local effect of the bars as a local form drag is stronger (Jalalabadi et al., 2021). The standing wave over the water surface does not contribute to PSC^+. The only significant term in DSS transport T^+ here is pressure transport ${T_p}$. Over the transitional roughness spacing, Fig. 5(e), the transport of DSS occurs only under the bar crest height through positive and negative T^+. In flow over larger bar spacing, Fig. 5(f), the standing wave over the water surface contributes to the positive T^+ while under the bar crest height T^+ acts mainly as a loss for DSS. As shown in Fig. 5, in flow over $\lambda/k=5.2$ the streamwise-averaged value of every dominant term is insignificant at almost every z/k thus both the DSS (Fig. 3(a)) and its contributors are negligible at all wall-normal distances from the bed. However, in flow over $\lambda/k=10.4$ Pressure–strain correlation and pressure transport largely contribute to the generation and damp of DSS both under and above the bar crest height.

The budgets of DARSS, $\left\langle\overline{u'w'}\right\rangle^+$, are calculated using Eq. (9) and shown in Fig. 6. Similar to the dispersive shear stress, dissipation (ε^+) and convection (C^+) terms are negligible and not shown here. The dominant terms are pressure–strain correlation (PSC^+) and transport (T^+) terms and the production (P^+) term is shown, although being considerably smaller than the dominant terms, for a comparison with Fig. 5(a,b). The dominant production term for DARSS is wake production, ${P_w}$, thus the total production terms shown in Fig. 6(a,b) are roughly equal to ${P_w}^+$. The distribution of ${P_w}^+$ in Fig. 6(a,b) are similar to those in Fig. 5(a,b) but with opposite sign. The regions of notable ${P_w}^+$ close to the leading edge of the bars in flow over $\lambda/k=5.2$ and those regions above the reattachement point and at the leading edge of the bars in flow over $\lambda/k=10.4$ occur at similar x/k and z/k for both DSS and DARSS. This reveals that the interplay between DSS and DARSS through wake production is similar to that between WKE and DATKE (Zampiron et al., 2021) although the value of this term is negligible here. In flow over transitional bar spacing, large contribution of PSC^+ in the generation of $\left\langle\overline{u'w'}\right\rangle^+$ are focused near the bed and bars crest height especially at the leading edge of them and slight undulation of water surface has small contribution to that. In flow over k-type bar spacing, the local large value of PSC^+ at the bar trailing edge extends to the bed and a strong positive contribution of PSC^+ is localized under the recirculation zone close to the bed. This is different with Fig. 5(d) and, considering the definition of PSC in Eqs. (8) and (9), it reveals that the recirculation zone mainly contributes to the temporal fluctuations of velocity and pressure but not to the spatial variations of these flow variables. The standing wave over the water surface contributes locally to the generation of PSC^+ too. The overall contribution of PSC^+ to DARSS is marked as generation as seen in Fig. 6(c,d) unlike that contribution to DSS. Similar to DSS, pressure transport ${T_p}$ has the main contribution to the transport of DARSS; however, this transport is not confined in the area below the bar crest in flow over $\lambda/k=5.2$. Transport of DARSS is mainly supported at the leading and trailing edge of the bars in this geometry and small undulations of the water surface contribute to this transport weakly. On the other hand, in flow over $\lambda/k=10.4$ bars contribute to transport of DARSS only mainly in their downstream while the water surface deformations have a major contribution to this transport. Positive and negative T^+ under the water surface represents the effects of surface wave on supporting

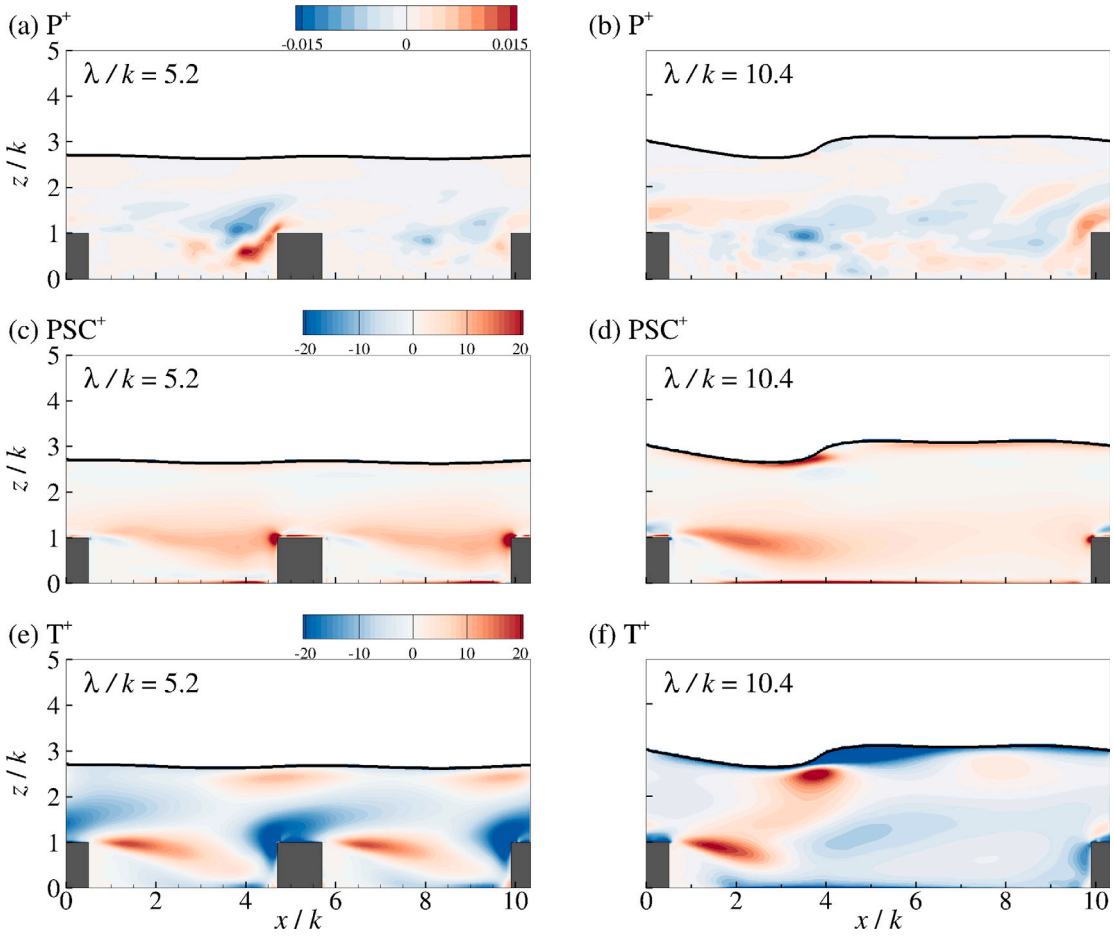

Fig. 6. Dominant terms of double-averaged Reynolds shear stress budget for (a,c,e) $\lambda/k = 5.2$ and (b,d,f) $\lambda/k = 10.4$.

and undermining DARSS transport. The local maxima of T^+ under the surface wave and at the downstream of the bar crest are connected and extended to bed in Fig. 6(f) representing the interaction of water surface, bar and bed in the transport of DARSS.

3.2. Wake kinetic energy and double-averaged turbulent kinetic energy budget

The budgets of wake kinetic energy and double-averaged turbulent kinetic energy are calculated using

$$\begin{aligned}\frac{1}{2}\frac{\partial\langle\widetilde{u}_i\widetilde{u}_i\rangle}{\partial t} &= \left[-\frac{1}{2}\langle\overline{u}_j\rangle\frac{\partial\langle\widetilde{u}_i\widetilde{u}_i\rangle}{\partial x_j}\right]_{\mathrm{C}}\\ &+\left[\left(-\langle\widetilde{u}_i\widetilde{u}_j\rangle\frac{\partial\langle\overline{u}_i\rangle}{\partial x_j}\right)_{\mathrm{P_s}}+\left(\langle\widetilde{u'_iu'_j}\frac{\partial\widetilde{u}_i}{\partial x_j}\rangle\right)_{\mathrm{P_w}}\right]_{\mathrm{P}}\\ &+\left[-\nu\langle\frac{\partial\widetilde{u}_i}{\partial x_j}\frac{\partial\widetilde{u}_i}{\partial x_j}\rangle\right]_{\varepsilon}\\ &+\left[\left(-\frac{1}{2}\frac{\partial\langle\widetilde{u}_i\widetilde{u}_i\widetilde{u}_j\rangle}{\partial x_j}\right)_{\mathrm{T_d}}+\left(-\langle\frac{\partial\widetilde{u'_iu'_j}\widetilde{u}_i}{\partial x_j}\rangle\right)_{\mathrm{T_w}}\right.\\ &\left.+\left(-\frac{1}{\rho}\langle\frac{\partial\widetilde{p}\widetilde{u}_i}{\partial x_i}\rangle\right)_{\mathrm{T_p}}+\left(\frac{1}{2}\nu\langle\nabla^2\widetilde{u}_i\widetilde{u}_i\rangle\right)_{\mathrm{T_\nu}}\right]_{\mathrm{T}}\end{aligned} \tag{10}$$

$$\begin{aligned}\frac{1}{2}\frac{\partial\langle\overline{u'_iu'_i}\rangle}{\partial t} &= \left[-\frac{1}{2}\langle\overline{u}_j\rangle\frac{\partial\langle\overline{u'_iu'_i}\rangle}{\partial x_j}\right]_{\mathrm{C}}\\ &+\left[\left(-\langle\overline{u'_iu'_j}\rangle\frac{\partial\langle\overline{u}_i\rangle}{\partial x_j}\right)_{\mathrm{P_s}}+\left(-\langle\widetilde{u'_iu'_j}\frac{\partial\widetilde{u}_i}{\partial x_j}\rangle\right)_{\mathrm{P_w}}\right]_{\mathrm{P}}\\ &+\left[-\nu\langle\overline{\frac{\partial u'_i}{\partial x_j}\frac{\partial u'_i}{\partial x_j}}\rangle\right]_{\varepsilon}\\ &+\left[\left(-\frac{1}{2}\frac{\partial\langle\overline{u'_iu'_iu'_j}\rangle}{\partial x_j}\right)_{\mathrm{T_t}}+\left(-\langle\frac{1}{2}\frac{\partial\widetilde{u}_j\widetilde{u'_iu'_i}}{\partial x_j}\rangle\right)_{\mathrm{T_w}}\right.\\ &\left.+\left(-\frac{1}{\rho}\langle\frac{\partial\overline{p'u'_i}}{\partial x_i}\rangle\right)_{\mathrm{T_p}}+\left(\nu\langle\nabla^2\overline{u'_iu'_i}\rangle\right)_{\mathrm{T_\nu}}\right]_{\mathrm{T}}\end{aligned} \tag{11}$$

The normalized dominant terms contributing to WKE, $1/2\langle\widetilde{u}_i\widetilde{u}_i\rangle$, are production P^+, transport T^+ and convection C^+ and shown in Figs. 7–9. These figures reveal that in flow over $\lambda/k = 5.2$ bars have the main role for consuming or producing WKE through the dominant terms in its budget. A seen in Fig. 7, the dominant production term for WKE is wake production $P_w{}^+$ in flow over transitional bar spacing while in flow over k-type bar spacing this is the shear production $P_s{}^+$ that contributes largely to P^+. This is due to the small variations of the mean velocities in flow over $\lambda/k = 5.2$ in all directions (note Eq. (10)) while these variations are not small in flow over $\lambda/k = 10.4$ at least in the streamwise direction (Jalalabadi et al., 2021). The standing wave over the water surface decreases WKE through negative production and the effects of bars on shear production $P_s{}^+$ is relatively large especially in and above the recirculation zone. The two dominant terms in transporting WKE are dispersive transport $T_d{}^+$ and wake transport $T_w{}^+$. Making the budget equations similar to the classical equations of Reynolds shear stress transport, the definition of wake transport here is different from that in previous works (Zampiron et al., 2021; Papadopoulos et al., 2019). The term defined here as dispersive transport $T_d{}^+$ is similar to turbulent transport but calculated using spatial variations of mean velocities. As seen in Fig. 8, the main redistribution

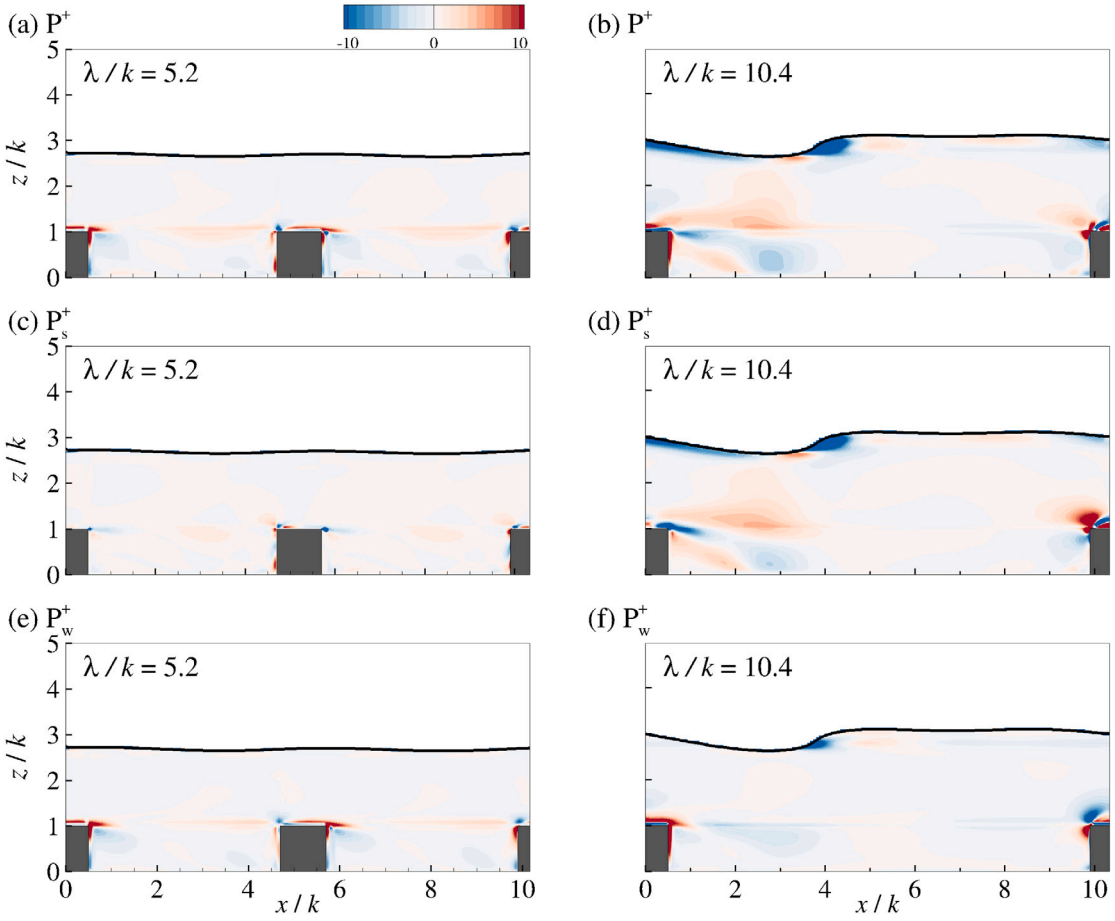

Fig. 7. Total production, shear production and wake production of wake kinetic energy for (a,c,e) $\lambda/k = 5.2$ and (b,d,f) $\lambda/k = 10.4$.

of WKE occurs around the bars meanwhile for larger bar spacing there is, as well, a significant redistribution of this energy at the downstream of the standing wave over the water surface through T_w^+. The main redistribution of WKE in flow over $\lambda/k = 5.2$ is provided by T_d^+ while both T_d^+ and T_w^+ have large contribution in redistribution of WKE around the bars in flow over $\lambda/k = 10.4$. In both geometries the bars induce strong generation and damping of WKE through convection term C^+ (Fig. 9); however, further above the bars in flow over $\lambda/k = 10.4$ the standing wave over the water surface contributes significantly to this term. This is attributed to the effects of large water surface deformation in generating significant spatial fluctuations of time-averaged velocities in the bulk flow. In flow over $\lambda/k = 5.2$ the small modulations over the water surface does not generate substantial spatial fluctuations of time-averaged flow variables. Regions of source and loss of C^+ under the water surface compensate each other in the streamwise direction so the mean C^+ is negligible at these wall-normal locations.

Fig. 10 shows the production terms that generate DATKE. Shear production P_s^+ is the significant term in both geometries as, considering the definition of this term in Eqs. (10), the time-averaged quantities and their fluctuations are larger than spatial fluctuations of time-averaged velocities and their variations. The standing wave over the water surface contributes to the production of DATKE via both P_s^+ and P_w^+ while contribution through the former is more notable. DATKE is extracted from the flow by the bars as P_w^+ around them is negative. Redistribution of DATKE is provided by turbulent, wake and pressure transport as shown in Fig. 11. The distribution of turbulent transport T_t^+ is roughly similar in both geometries except that it is stronger in flow over $\lambda/k = 10.4$ at bar crest height and the standing wave over water surface is a source of loss and gain in small regions at its downstream. Transport due to wake T_w^+ is also large under the standing wave over the water surface due to the large spatial fluctuations of time-averaged velocities induced by this wave. Pressure transport T_p^+, on the other hand, is the largest term of T^+ in flow over $\lambda/k = 5.2$ since the stable vortex formed between the bar at this small bar spacing leads to larger fluctuations of pressure and velocity at the bars edges. Large contribution of pressure transport in DATKE redistribution compared to insignificant effects of pressure in the redistribution of WKE is attributed to the large temporal fluctuations of mean velocity and pressure than spatial fluctuations of velocity and pressure. It is seen in Fig. 12 that, similar to Fig. 9 for WKE, convection C^+ is a notable term in consumption and production of DATKE and bars are the main source of large positive and negative C^+ regardless of their distance. However; the extraction of DATKE is stronger at the downstream of the bar in flow over $\lambda/k = 10.4$ and another notable loss of $1/2\left\langle\overline{u'w'}\right\rangle^+$ is induced by the standing wave. There is a large interaction between bar crest and standing wave in terms of negative convection and a large interaction between the reattachement area over the bed and upstream of the standing wave in terms of positive convection. In Figs. 10–12 the regions of gain and loss of different contributions to DATKE do not counterbalance each other so the streamwise-averaged contributions are not negligible.

4. Conclusions

The effects of roughness and water surface deformation on rms velocity fluctuations, dispersive and double-averaged Reynolds shear stress as well as wake and double-averaged turbulent kinetic energy in open channel flow over a rough bed have been investigated. Spanwise-aligned square bars attached to the wall are considered as roughness

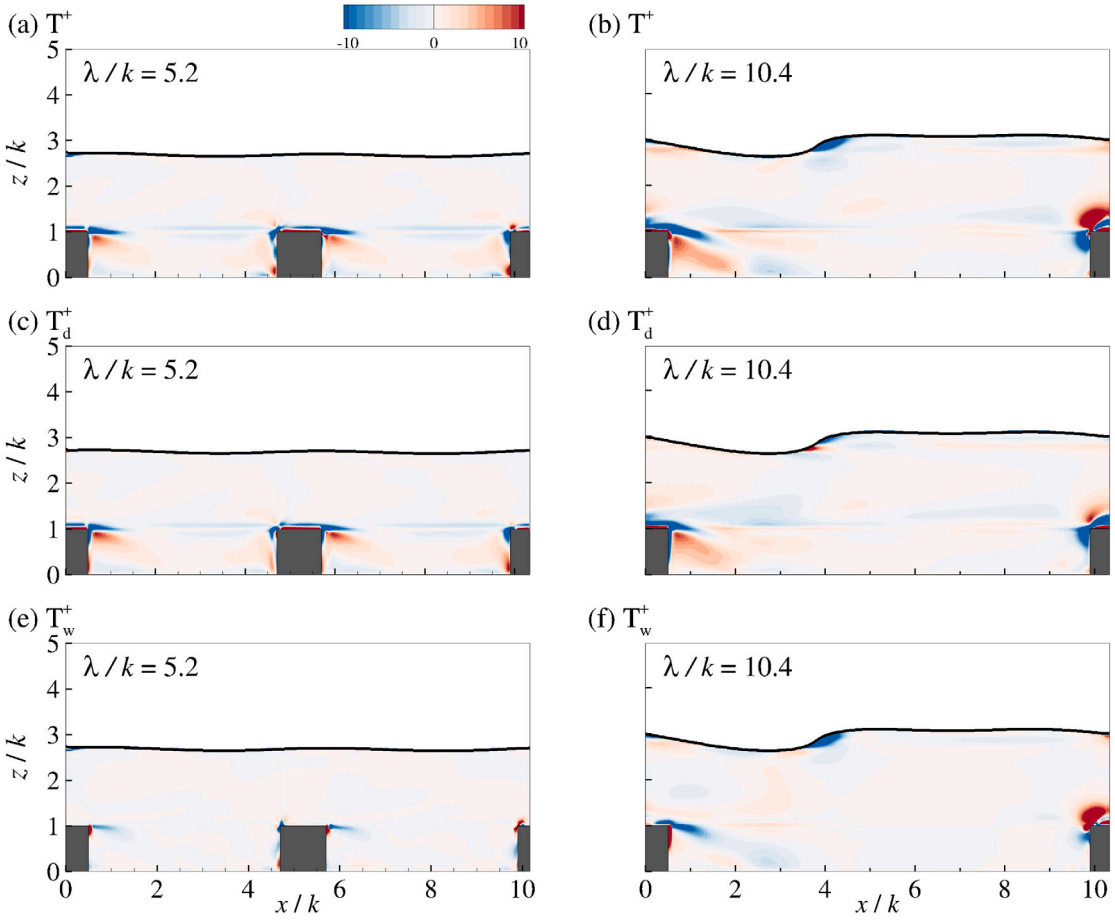

Fig. 8. Total transport, dispersive transport and transport due to wake of wake kinetic energy for (a,c,e) $\lambda/k = 5.2$ and (b,d,f) $\lambda/k = 10.4$.

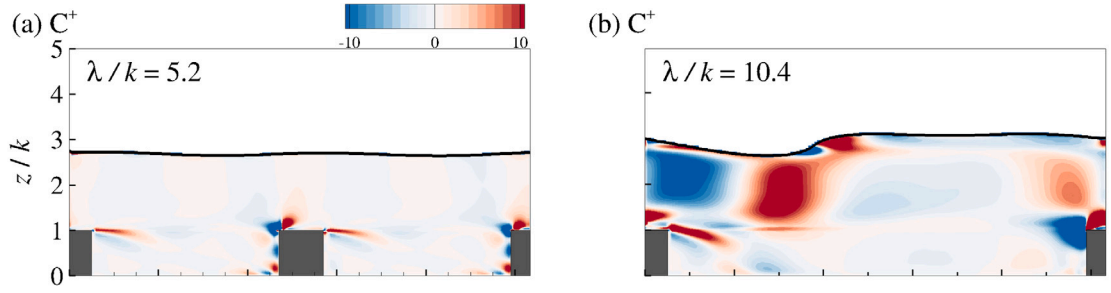

Fig. 9. Convection of wake kinetic energy for (a) $\lambda/k = 5.2$ and (b) $\lambda/k = 10.4$.

and the results of large-eddy simulations are used for this purpose. The bar spacings correspond to transitional and k-type roughness; while in the former a stable vortex is formed between bars, a recirculation zone is generated at the downstream of the bar that extends to a reattachment point and a standing wave is developed over the water surface in the latter. The main peak of all first and second order statistics occurs at around the bar crest height. The standing wave developed at the water surface in flow over k-type bar spacing generates a second peak under the water surface in the streamwise rms velocity. The second peak under the water surface in the spanwise velocity profile is similar in strength and location for flows in both geometries thus its presence is only due to the water surface not its specific deformations. Wall-normal rms velocity profiles do not exhibit a major second peak under the water surface in both geometries. This second peak is, as well, present in the dispersive and double-averaged Reynolds shear stress and wake and double-averaged turbulent kinetic energy in flow over k-type roughness. Due to the standing wave at the water surface the dispersive shear stress and wake kinetic energy are notable above the bar in the bulk of the flow as this standing wave induces spatial fluctuations in the time-averaged flow quantities. Sweep and ejection events, dominant in the generation of the shear stress, exhibit similar contributions to the double-averaged Reynolds shear stress in both geometries with sweeps being strongest under the bar crest and ejections the strongest above that height. This is reversed for the dispersive shear stress suggesting the opposite sign of the components of dispersive and double-averaged Reynolds shear stress. The budgets of the dispersive shear stress are explored and show that the non-negligible terms in the budgets are pressure-strain correlation and transport terms. Pressure-strain correlation is significant close to the bed and edges of the bars as the pressure variations in these areas are large. Pressure transport is the major source of loss and gain for the dispersive shear stress and have large values only under the bar crest in flow over transitional roughness. Over k-type roughness the standing wave at the water surface contributes significantly to the pressure

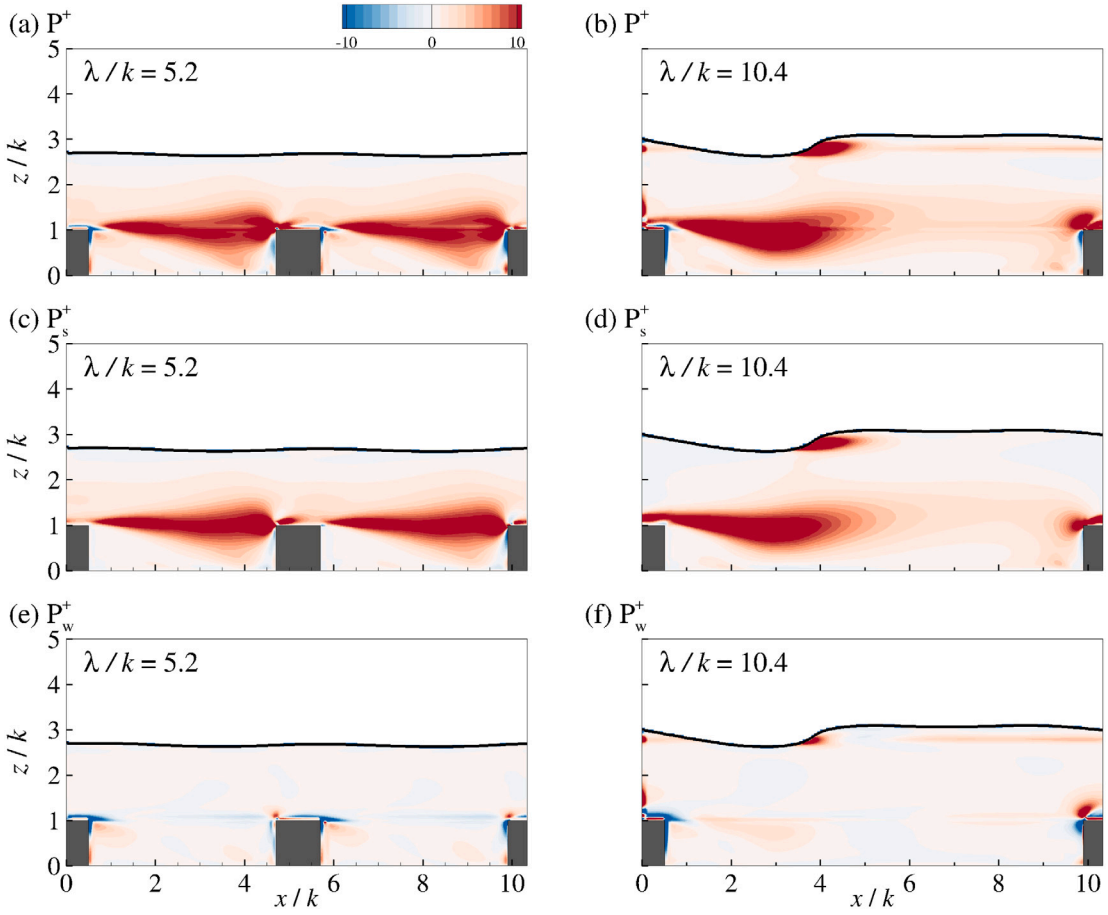

Fig. 10. Total production, shear production and wake production of double-averaged turbulent kinetic energy for (a,c,e) $\lambda/k = 5.2$ and (b,d,f) $\lambda/k = 10.4$.

transport. The streamwise-averaged components of dispersive shear stress are negligible. The dominant terms of double-averaged Reynolds shear stress budget are, as well, pressure-strain correlation and pressure transport. Unlike in the dispersive shear stress, these dominant terms are not confined under the bar crest as the components of these contributions are mainly the temporal fluctuations of velocity and pressure. In addition to the bars, the standing wave at the water surface contributes locally to the generation of pressure-strain-correlation too. This standing wave contributes considerably to pressure transport as well which is the major transport term that redistributes double-averaged Reynolds shear stress. The dominant term contributing to both wake kinetic energy and double-averaged kinetic energy are production, transport and convection. In wake kinetic energy, wake production constitute the main source for production in flow over transitional bar spacing while in flow over k-type bar spacing shear production is the larger contributor to total production at the bar crest and under the standing wave. Dispersive transport represents the spatial variation of all mean velocities and along with wake transport contributes mainly to the total transport of wake kinetic energy. The effects of standing wave at the water surface is considerable in the convection of wake kinetic energy. Unlike wake kinetic energy, shear production is the major term of total production in both geometries for double-averaged Reynolds shear stress. For this shear stress turbulent, wake and pressure transport redistribute the energy but their values are smaller than convection and production. Large interaction of the water surface, bed and bars are seen in the convection of double-averaged Reynolds shear stress. The results in the present work reveal that the role of dissipation in extracting the energy that enters the flow is diminished for the double-averaged shear stress and kinetic energy while all other terms contribute to the gain and loss of energy. It should be noted that the budget equations in the current work are derived for a constant geometry function and without this condition new terms will emerge in these equations. Carrying out similar analysis in flow over roughness with a varying geometry function in wall-normal direction and with spanwise heterogeneity will reveal the effects of roughness topography in the distribution of flow statistics and budgets of shear stresses and kinetic energies. This will be beneficial for better understanding and prediction of flow hydrodynamics in natural and man-made geometries including rivers, sewerage systems and canals.

CRediT authorship contribution statement

Razieh Jalalabadi: Conceptualization, Investigation, Simulation, Formal analysis, Writing. **Thorsten Stoesser:** Conceptualization, Funding acquisition, Writing – review & editing.

Declaration of competing interest

The authors declare that they have no known competing financial interests or personal relationships that could have appeared to influence the work reported in this paper.

Data availability

Data will be made available on request.

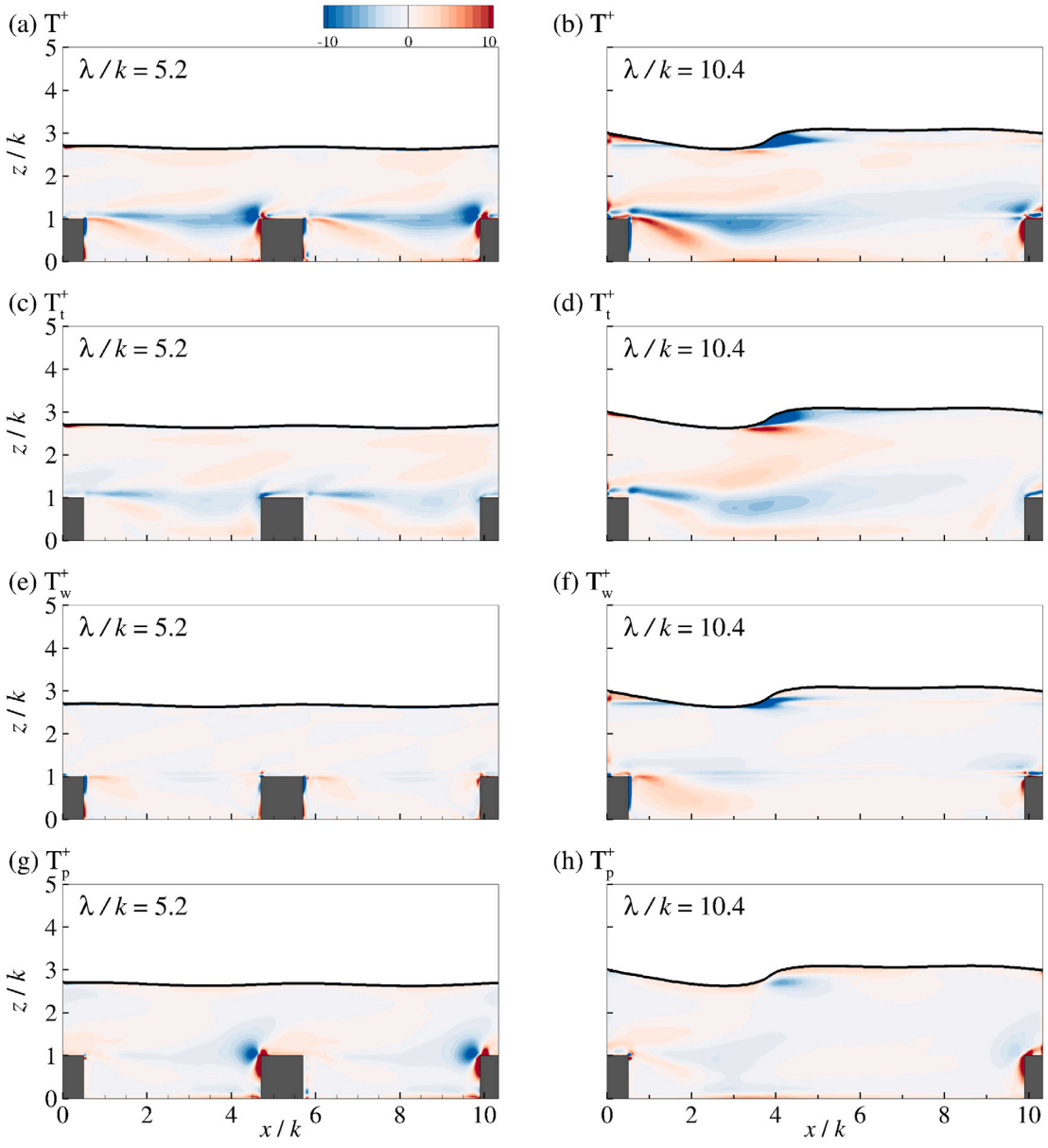

Fig. 11. Total transport, turbulent transport, transport due to wake and pressure transport of double-averaged turbulent kinetic energy for (a,c,e) $\lambda/k = 5.2$ and (b,d,f) $\lambda/k = 10.4$.

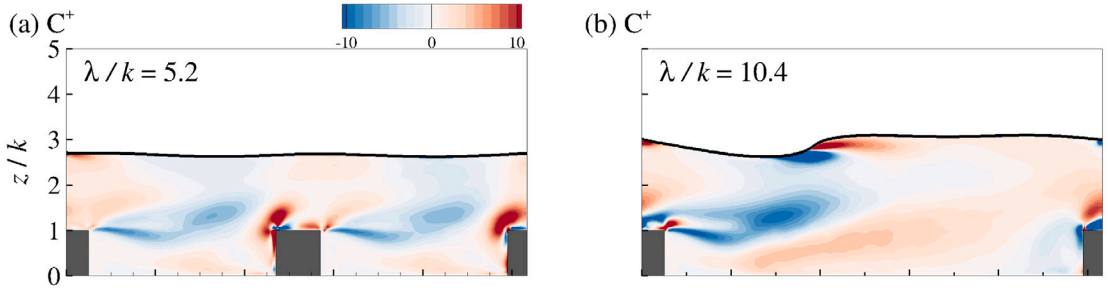

Fig. 12. Convection of double-averaged turbulent kinetic energy for (a) $\lambda/k = 5.2$ and (b) $\lambda/k = 10.4$.

Acknowledgements

Financial support was provided by the EPSRC/UK project "Rapid Monitoring of River Hydrodynamics and Morphology using Acoustic Holography", grant number EP/R022135/1. The fine-grid and large-domain large-eddy simulations were carried out on UCL's high performance computer Grace.

References

Abe, H., Kawamura, H., Matsuo, Y., 2001. Direct numerical simulation of a fully developed turbulent channel flow with respect to the Reynolds number dependence. ASME J. Fluids Eng. 123, 382.

Antonia, R.A., Kim, J., 1994. Low-Reynolds-number effects on near-wall turbulence. J. Fluid Mech. 276, 61.

Ashrafian, A., Andersson, H.I., 2006. The structure of turbulence in a rod-roughened channel. Intl. J. Heat Fluid Flow 27, 65.

Blackman, K., Perret, L., Calmet, I., Rivet, C., 2017. Turbulent kinetic energy budget in the boundary layer developing over an urban-like rough wall using PIV. Phys. Fluids 29 (8), 85.

Castro, I.P., Cheng, H., Reynolds, R., 2006. Turbulence over urban-type roughness: deductions from wind-tunnel measurements. Bound.-Layer Meteorol. 118 (1), 109.

Coleman, G., Kim, J., Spalart, P., 2003. Direct numerical simulation of a decelerated wall-bounded turbulent shear flow. J. Fluid Mech. 495, 1.

Cui, J., Patel, V.C., Lin, C.L., 2003. Large-eddy simulation of turbulent flow in a channel with rib roughness. Int. J. Heat Fluid Flow 24, 372.

Djenidi, L., Elavarasan, R., Antonia, R.A., 1999. The turbulent boundary layer over transverse square cavities. J. Fluid Mech. 395, 271–294.

Dwyer, M.J., Patton, E.G., Shaw, R.H., 1997. Turbulent kinetic energy budgets from a large-eddy simulation of airflow above and within a forest canopy. Bound.-Layer Meteorol. 84 (1), 23.

Finnigan, J., 2000. Turbulent in plant canopies. Annu. Rev. Fluid Mech. 32 (1), 519.

Forooghi, P., Stroh, A., Schlatter, P., Frohnapfel, B., 2018. Direct numerical simulation of flow over dissimilar, randomly distributed roughness elements: A systematic study on the effect of surface morphology on turbulence. Phys. Rev. Fluids 3, 044605.

Giometto, M.G., Christen, A., Meneveau, C., Fang, J., Krafczyk, M., Parlange, M.B., 2016. Spatial characteristics of roughness sublayer mean flow and turbulence over a realistic urban surface. Bound.-Layer Meteorol. 160 (3), 425.

Hoyas, S., Jiménez, J., 2008. Reynolds number effects on the Reynolds-stress budgets in turbulent channels. Phys. Fluids 20, 101511.

Ikeda, T., Durbin, P., 2007. Direct numerical simulations of a rough-wall channel flow. J. Fluid Mech. 571, 235–263.

Jalalabadi, R., Stoesser, T., 2022. Reynolds and dispersive shear stress in free-surface turbulent channel flow over square bars. Phys. Rev. E 105, 035102.

Jalalabadi, R., Stoesser, T., Ouro, P., Luo, Q., Xie, Z., 2021. Free surface flow over square bars at different Reynolds numbers. J. Hydro-Environ. Res. 36, 64.

Jelly, T.O., Busse, A., 2018. Reynolds and dispersive shear stress contributions above highly skewed roughness. J. Fluid Mech. 852, 710.

Jelly, T.O., Busse, A., 2019. Reynolds number dependence of Reynolds and dispersive stresses in turbulent channel flow past irregular near-Gaussian roughness. Intl. J. Heat Fluid Flow 80, 108485.

Jiménez, J., 2004. Turbulent flows over rough walls. Annu. Rev. Fluid Mech. 36 (4), 15.

Kara, S., Kara, M.C., Stoesser, T., Sturm, T.W., 2015. Free-surface versus rigid-lid LES computations for bridge-abutment flow. J. Hydraul. Eng. 141 (9), 04015019.

Komminaho, J., Skote, M., 2002. Reynolds stress budgets in couette and boundary layers. Flow, Turbul. Combust. 68, 167.

Krogstad, P.A., Andersson, H.I., Bakken, O.M., Ashrafian, A., 2005. An experimental and numerical study of channel flow with rough walls. J. Fluid Mech. 530, 327.

Manes, C., Pokrajac, D., Coceal, O., McEwan, I., 2008. Significance of form-induced stress in rough wall turbulent boundary layers. Acta Geophys. 56, 845.

Mansour, N.N., Kim, J., Moin, P., 1988. Reynolds-stress and dissipation-rate budgets in a turbulent channel flow. J. Fluid Mech. 194, 173.

McSherry, R., Chua, K., Stoesser, T., Mulahasan, S., 2018. Free surface flow over square bars at intermediate relative submergence. J. Hydraul. Res. 56 (6), 825.

Nezu, I., Nakagawa, H., 1993. Turbulence in open-channel flows. In: IAHR monograph, Balkema, Rotterdam, The Neatherlands.

Nicoud, F., Ducros, F., 1999. Subgrid-scale stress modelling based on the square of the velocity gradient tensor. Flow Turbul. Combust. 62 (3), 183.

Nikora, V.I., McEwan, I., McLean, S., Coleman, S., Pokrajac, D., Walters, R., 2007. Double-averaging concept for rough-bed open-channel and overland flows: Theoretical background. J. Hydraul. Eng. 133, 873.

Orlandi, P., Pirozzoli, S., 2021. Secondary flow in smooth and rough turbulent circular pipes: Turbulence kinetic energy budgets. Fluids 6, 448.

Papadopoulos, K., Nikora, V., Cameron, S., Stewart, M., Gibbins, C., 2019. Spatially-averaged flows over mobile rough beds: equations for the second-order velocity moments. J. Hydraul. Res. 58, 133.

Pokrajac, D., Campbell, L.J., Nikora, V., Manes, C., McEwan, I., 2007. Quadrant analysis of persistent spatial velocity perturbations over square-bar roughness. Exp. Fluids 42, 413.

Raupach, M.R., Shaw, R.H., 1982. Averaging procedures for flow within vegetation canopies. Bound.-Lay. Meteorol. 22 (1), 79–90.

Sethian, J.A., Smereka, P., 2003. Level set methods for fluid interfaces. Annu. Rev. Fluid Mech. 35, 146.

Spalart, P., 1988. Direct simulation of a turbulent boundary layer up to Re_τ=1410. J. Fluid Mech. 187, 61.

Stoesser, T., Rodi, W., 2007. Large eddy simulation of open-channel flow over spheres. In: High Performance Computing in Science and Engineering '06. Springer, Berlin, Heidelberg.

Tian, G., Conan, B., Calmet, I., 2020. Turbulence-kinetic-energy budget in the urban-like boundary layer using large-eddy simulation. Bound.-Layer Meteorol. 178, 201.

Toussaint, D., Chedevergne, F., Léon, O., 2020. Analysis of the different sources of stress acting in fully rough turbulent flows over geometrical roughness elements. Phys. Fluids 32, 075107.

Wallace, J.M., 2016. Quadrant analysis in turbulence research: history and evolution. Annu. Rev. Fluid Mech. 131, 131.

Wilson, N.R., Shaw, R.H., 1977. A higher order closure model for canopy flow. J. Appl. Meteorol. 16, 1197.

Yuan, J., Piomelli, U., 2014. Roughness effects on the Reynolds stress budgets in near-wall turbulence. J. Fluid Mech. 760, R1–1.

Zampiron, A., Cameron, S., Nikora, V., 2021. Momentum and energy transfer in open-channel flow over streamwise ridges. J. Fluid Mech. 915, A42.